

An Accretion Flare Interpretation for the Ultra-High-Energy Neutrino Event KM3-230213A

CHENGCHAO YUAN (袁成超),¹ LEONARD PFEIFFER,² WALTER WINTER,¹ SARA BUSON,^{1,2} FEDERICO TESTAGROSSA,¹
JOSE MARIA SANCHEZ ZABALLA,² AND ALESSANDRA AZZOLLINI²

¹*Deutsches Elektronen-Synchrotron DESY, Platanenallee 6, 15738 Zeuthen, Germany*

²*Julius-Maximilians-Universität Würzburg, Fakultät für Physik und Astronomie, Institut für Theoretische Physik und Astrophysik, Lehrstuhl für Astronomie, Emil-Fischer-Straße 31, 97074 Würzburg, Germany*

ABSTRACT

We study the origin of the ultra-high-energy (UHE) neutrino event KM3-230213A detected by KM3NeT, focusing on MRC 0614-083 which has been pinpointed as the closest blazar to the neutrino localization. A joint interpretation of the optical, infrared, and X-ray light curves suggests that MRC 0614-083 has undergone a super-Eddington accretion flare accompanied by efficient proton acceleration. That flare has initiated a delayed infrared echo within the surrounding dust torus, which serves as a target for photomeson ($p\gamma$) interactions such that a self-consistent picture emerges: the predicted UHE neutrino flux is at the level expected from joint E^{-2} fit with the IceCube measurements at lower energies, the variable nature of the event alleviates the tension with IceCube limits, and the accompanying electromagnetic cascade describes the X-ray flare around the neutrino detection time. Since a key remaining uncertainty is the unknown redshift of the source, we strongly encourage optical/ultraviolet spectroscopic measurements to determine its redshift.

Keywords: Neutrino astronomy; active galaxies; radiative processes

1. INTRODUCTION

The KM3NeT neutrino observatory in the Mediterranean Sea (Adrian-Martinez et al. 2016) has recently reported the detection of the ultra-high-energy (UHE) neutrino event KM3-230213A in the near-horizontal direction with an energy of 220 PeV (72 PeV – 2.6 EeV at the 90% CL; Aiello et al. 2025). This extraordinary event thereby extends the energy range of neutrino astronomy into the UHE domain, which means that the associated primary was an Ultra-High-Energy Cosmic Ray (UHECRs) exceeding EeV energies. Identifying the astrophysical source of KM3-230213A would be truly spectacular, as this may be the first direct evidence for the origin of UHECRs. Discussed possible origins (Adriani et al. 2025a,b; Muzio et al. 2025; Neronov et al. 2025; Fang et al. 2025; Dzhathdov 2025; Das et al. 2025; Zhang et al. 2025) include (steady or transient) extragalactic sources, Galactic sources, or a cosmogenic origin from interactions between UHECRs and background photons in the Universe. However, the non-detection of neutrinos at such energies by IceCube (Abbasi et al. 2025;

Adriani et al. 2025c; Li et al. 2025) results in a tension at a high confidence level ($\gtrsim 3\sigma$) for the diffuse cosmogenic scenario, given IceCube’s larger effective area and longer operational period. It has been also pointed out that the tension can be alleviated to $2 - 3\sigma$ assuming a transient point source (e.g., Li et al. 2025; Neronov et al. 2025).

Accompanying the discovery of KM3-230213A, 17 blazars located within the 99% containment region have been identified as potentially correlated with the UHE neutrino event (Adriani et al. 2025b). Seven of these blazars have been identified through X-ray, infrared, and radio cross-matches. Among them, MRC 0614-083 is the closest object located only 0.6° away from the best-fit neutrino position (the only blazar within the 68% CL region). It exhibits an X-ray flare observed by the Swift X-Ray Telescope (XRT; Burrows et al. 2005) and eROSITA (Merloni et al. 2024) around the time of the neutrino detection. Additionally, optical observations from the Asteroid Terrestrial-impact Last Alert System (ATLAS; Tonry et al. 2018), the Catalina Real-Time Transient Survey (CRTS; Drake et al. 2009), and the Zwicky Transient Facility (ZTF; Masci et al. 2019), along with infrared observations from the Wide-field Infrared Survey Explorer (WISE; Wright et al. 2010) and

Near-Earth Object WISE (NEOWISE; Mainzer et al. 2011), have revealed variable features in the light curves prior to the neutrino’s arrival, suggesting potential interconnections.

Motivated by the time delays between the peaks of the optical and infrared light curves, as well as the possible coincidence of the neutrino detection with the X-ray flare, we propose an accretion flare model for the blazar MRC 0614-083, in which protons accelerated during the optical flare phase – associated with enhanced accretion activity – produce neutrinos and trigger electromagnetic cascades. We aim to provide a self-consistent interpretation of the infrared and X-ray flares, while establishing a connection between the flaring state and the UHE neutrino event. In this model, the optical light curve will be treated as a proxy for the time evolution of the accretion rate onto the supermassive black hole (SMBH). Such activity may originate from enhanced accretion of ambient molecular gas. The dust torus surrounding the SMBH, with a radius of approximately $\sim 10^{17} - 10^{18}$ cm (e.g., Ghisellini et al. 2017), can absorb the optical emission and re-radiate it in the infrared bands, producing so-called dust echoes (e.g., Lu et al. 2016; Jiang et al. 2016).

In the context of active galactic nuclei (AGN), besides extended relativistic jets, the particle accelerators could be structures within the inner edge of the dust torus, such as accretion disks (e.g., Murase & Stecker 2023, for review), sub-relativistic winds (Wang & Loeb 2017; Liu et al. 2018), disk coronae (Murase et al. 2020; Fiorillo et al. 2024), or inner jets (Murase et al. 2012; Murase et al. 2014). In this work, without loss of generality, we do not specify the exact acceleration mechanism, but instead inject protons into an isotropic radiation zone. In the radiation zone, characterized by the radius of the dust torus (such as the non-relativistic winds reaching the inner edge of the dust torus), $p\gamma$ interactions between injected protons and thermal optical and infrared photons can produce UHE neutrinos and initiate electromagnetic (EM) cascades (e.g., Yuan & Winter 2023). The resulting neutrino emission can reach UHE ranges, and the accompanying X-ray emission may account for the observed neutrino flare. One caveat is that the redshift (z) of the blazar remains unknown; however, for completeness, we investigate how the outcomes of this model depend on redshift by varying z from 0.5 to 2.0.

Throughout the paper, the time and energy measured in the SMBH-rest frame are denoted as t and ε , which are related to the quantities in the observer’s frame through $t = T_{\text{obs}}/(1+z)$ and $\varepsilon = (1+z)E$. We assume a standard Λ CDM universe with matter density $\Omega_m = 0.3$ and Hubble constant $H_0 = 71.9 \text{ km s}^{-1} \text{ Mpc}^{-1}$

(Bonvin et al. 2017). The notation Q_x represents $Q/10^x$ in CGS units unless otherwise specified.

2. MULTI-WAVELENGTH OBSERVATIONS AND INFRARED ECHOES

2.1. Multi-wavelength observations

This study combines archival multi-wavelength data with newly acquired X-ray observations to construct the spectral and temporal profile of MRC 0614-083. This source is detected in several radio surveys¹, however, these observations are treated as upper limits in our model because the radio emission is likely associated with (extended) jet structures rather than the accretion-related region.

In infrared (IR) and optical wavelengths we incorporate observations from WISE (W1, W2, W3 and W4 filters) and NEOWISE (W1, W2; identical to WISE) as well as ATLAS (cyan c filter) and ZTF (red r and green g bands), covering the period from 2018 to early 2025. Fig.1 highlights the ZTF r -band (blue) and NEOWISE W2-band (red) light curves, shown in the first and second panels, respectively. Observations in the W3 and W4 filters are only available from the original WISE mission from 2009 to early 2011, since these bands were not used in later phases of the survey due to detector saturation. The magnitudes are corrected for galactic extinction and translated to energy flux units using the source-dependent reddening value between the B- and V-band, $E(B-V)$, from Schlafly & Finkbeiner (2011) with the extinction law adapted from Fitzpatrick (1999).

The X-ray coverage includes both archival data from eROSITA and Swift-XRT and new Target of Opportunity (ToO) observations carried out with Swift-XRT on the 9th of April 2025, coordinated following the neutrino detection. These data sets were uniformly reprocessed using the procedure discussed in Adriani et al. (2025b). The eROSITA and Swift-XRT light curve, in an energy range of 0.2 – 2.3 keV, is displayed together in the bottom panel of Fig. 1. We furthermore provide a 3σ upper limit from XMM-Newton² at MJD 60410.

While optical photometry and broadband spectral energy distribution (SED) data are available, no optical spectra from slit spectroscopy are publicly accessible for

¹ Rapid ASKAP Continuum Survey (RACS; Hale et al. 2021), NRAO VLA Sky Survey (NVSS; Condon et al. 1998), Very Large Array Sky Survey (VLASS; Gordon et al. 2021), Very Large Array Low-frequency Sky Survey Redux (VLLSR; Lane et al. 2014), Molonglo Reference Catalogue of Radio Sources (MRC; Large et al. 1991), and the Parkes-MIT-NRAO radio continuum survey (PMN; Wright et al. 1994)

² The XMM-Newton X-ray upper limit is obtained from <http://xmmuls.esac.esa.int/upperlimitserver/>

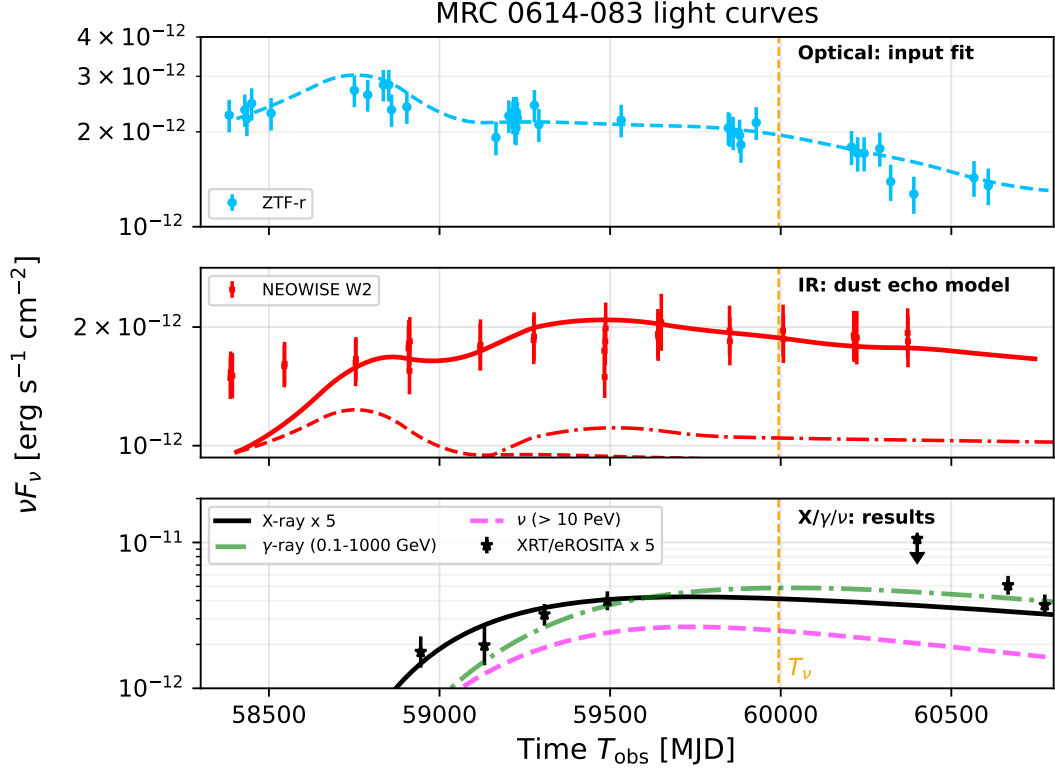


Figure 1. Observed multi-wavelength light curves of MRC 0614083. Top panel: ZTF optical (r-band) observations (blue points) and the interpolated optical light curve (blue dashed curve). Middle panel: Infrared W2-band data from NEOWISE (red points) with the dust echo fit (solid red curve). The early-time and spherical components are shown as red dashed and red dash-dotted curves, respectively. Bottom panel: X-ray observations (black points) and results. The cascade X-ray and γ -ray light curves are shown as the black solid and green dashed-dotted curves, respectively, while the magenta dashed curve represents the light curve of single-flavor neutrinos with energies above 10 PeV. The vertical orange dashed line depicts the neutrino detection time T_ν . Data sources are listed in the main text.

MRC 0614-083, preventing the detection of emission or absorption lines and thus a direct redshift measurement. The initial approach was to constrain the redshift photometrically using ultraviolet (UV) observations from Swift Ultraviolet/Optical Telescope (UVOT) in multiple filters, following the methods from [Rau et al. \(2012\)](#). This technique relies on the redshift-dependent onset of Lyman-alpha absorption, which causes a characteristic flux suppression in UV to optical wavelengths. Hence, we requested additional Swift observations as a target of opportunity (ToO ID: 22343) to explore this approach. The UVOT data were processed following standard procedures, using `uvotimsum` to co-add images from individual exposures and `uvotsource` to determine fluxes and magnitudes. However, the UV data only yield non-detections; we report 3σ upper limits in each UVOT band, offering no constraint on the Lyman-alpha break and leaving ambiguity as to whether the source is intrinsically faint in the UV or fully absorbed. Determining the redshift of this source is essential, as it directly im-

pacts the luminosity scale in the joint SED fitting process. We therefore advocate for targeted spectroscopic observations at optical or UV wavelengths to obtain this key parameter.

High energy gamma-ray data was extracted from the light curve published in [Adriani et al. \(2025b\)](#), obtained with the *Fermi* Large Area Telescope (LAT). The data analysis presented in the light curve only yields upper limits with no significant flux detected around the time of the neutrino event. Based on the provided energy range (0.1 – 1000 GeV), we computed an upper limit on the gamma-ray energy flux at the time of the neutrino event, which serves to constrain the high energy contribution of the AGN modeling.

To construct the final broadband SED, we averaged the fluxes from the archival and newly acquired light curves in each band and placed the resulting energy fluxes at the effective frequencies corresponding to their respective filters or pass bands. The orange, red and blue points in Fig. 2 represent the radio,

IR/optical/UV, and X-ray regimes, respectively, complementing the *Fermi*-LAT γ -ray upper limit in green. The IR and optical spectra can be described as two blackbody components with temperatures of $k_B T_{\text{IR}} \sim 0.1$ eV and $k_B T_{\text{Opt}} \sim 1.5 - 2.0$ eV, respectively, in the observer's frame (see the dashed gray curve in Fig. 2). Based on these characteristic temperatures and the light curves in the r -band and W2-band, we estimated the bolometric luminosities using the relation $L_i = 4\pi d_L^2(z) \mathcal{C}_{i,\text{bol}}[\nu F_{\nu,i}]$, where $i = \text{IR}$ and Opt correspond to the IR and optical bands, d_L is the luminosity distance, and $\mathcal{C}_{i,\text{bol}}$ denotes the bolometric correction factor, defined as the ratio of the total energy flux of the blackbody distribution to the flux of the observed energy band. The bolometric IR and optical luminosities will be used in the dust echo fitting and multimessenger modeling presented in subsequent Sections, while the X-ray observations will be interpreted as the outputs of our model.

2.2. IR: dust echoes

Multi-wavelength observations indicate that the infrared spectrum (e.g., the first red point above 0.1 eV in Fig. 2) can be described by a blackbody distribution, in contrast to the soft component observed below 0.1 eV. The thermal shape of the spectrum, the gradually rising IR light curves, and the delayed IR emission relative to the optical emission all support a dust echo origin, similar to that seen in neutrino-emitting tidal disruption events (TDEs; Reusch et al. 2022; van Velzen et al. 2024; Li et al. 2024), where IR photons are emitted by a dust torus heated by optical radiation from the inner regions such as the accretion disk. The temperature of the IR-emitting dust is limited by the dust sublimation temperature, $\varepsilon_{\text{IR}} = k_B T_{\text{sub}} \sim 0.16$ eV, implying a peak IR energy in the observer's frame of $E_{\text{IR}} \lesssim 3.92\varepsilon_{\text{IR}}/(1+z) \simeq 0.63$ eV/(1+z)³, consistent with the observed IR data. Within the dust echo framework, the radius of the dust torus can be estimated as $R_{\text{IR}} \sim \Delta T_{\text{IR}} c/[2(1+z)] \simeq 1.1 \times 10^{18}$ cm/(1+z), where $\Delta T_{\text{IR}} \sim 850$ d is the observed delay of the IR emission with respect to the optical peak.

To fit the IR light curve, we follow the treatment in Winter & Lunardini (2023); Yuan et al. (2024) for neutrino emitting TDEs and define the generic time-spreading function $f(t) = f_{\text{ET}} + f_{\text{S}}$, where $f_{\text{ET}}(t) = \alpha\delta(t)$ and $f_{\text{S}} = (1-\alpha)H(t, 0, \Delta t_{\text{IR}})/\Delta t_{\text{IR}}$ respectively represent the contributions from the early-time com-

ponent⁴ and the spherical dust torus. In this expression, $0 \leq \alpha \leq 1$ denotes the fraction of the total IR power attributed to line-of-sight dust, which is modeled by the Dirac delta function $\delta(t)$. The boxcar function $H(t, 0, \Delta t_{\text{IR}})$ is defined such that $H(t, 0, \Delta t_{\text{IR}}) = 1$ for $0 \leq t \leq \Delta t_{\text{IR}}$ and $H(t, 0, \Delta t_{\text{IR}}) = 0$ otherwise, and is commonly used to describe the torus contribution. The bolometric IR luminosity L_{IR} is then obtained as the convolution of the bolometric optical luminosity L_{Opt} with the time-spreading function $f(t)$,

$$L_{\text{IR}}(t) = \epsilon_{\text{dust}} \int_{-\infty}^{+\infty} L_{\text{Opt},0}(t') f(t-t') dt', \quad (1)$$

where $\epsilon_{\text{dust}} < 1$ is the fraction of the incident optical radiation that is reprocessed to IR radiation by the illuminated dust and $L_{\text{Opt},0} = L_{\text{Opt}}/(1-\epsilon_{\text{dust}})$ is the optical luminosity before dust absorption. Here, $f(t)$, $L_{\text{IR}}(t)$, and $L_{\text{Opt},0}(t)$ are defined in terms of time (t) measured in the SMBH-rest frame, which is related to the time in observer's frame via $t = T_{\text{obs}}/(1+z)$.

Using L_{IR} and L_{Opt} obtained before, the energy released in the IR and optical bands can be expressed as $\mathcal{E}_{\text{IR}} = \int L_{\text{IR}} dt$ and $\mathcal{E}_{\text{Opt}} = \int L_{\text{Opt}} dt$. This allows us to approximate ϵ_{dust} as the ratio of the IR bolometric energy to the total energy in optical and IR bands, i.e., $\epsilon_{\text{dust}} \approx \mathcal{E}_{\text{IR}}/(\mathcal{E}_{\text{Opt}} + \mathcal{E}_{\text{IR}}) \simeq 0.37$. We fix $\epsilon_{\text{dust}} = 0.37$ and apply Eq. 1 to fit the NEOWISE W2 light curve (shown as the solid red curve in the middle panel of Fig. 1), yielding $\alpha \simeq 0.45$. The dashed and dashed-dotted curves respectively indicate the early-time and spherical dust torus components, assuming a reference redshift of $z = 0.5$. We restrict our fit to times after the optical peak, as IR emission before 58500 MJD likely stems from earlier optical activity and is less relevant to KM3NeT's neutrino detection window. The underestimated IR emission before 58500 MJD does not significantly affect the neutrino flux. As will be shown later, the source is optically thick to $p\gamma$ interactions. We note that the uncertainty in dust echo fit due to z is not significant, as the luminosities are directly inferred from observations and scale with the luminosity distance in the same way.

3. MULTIMESSENGER MODELING

3.1. Model description

The peak of the optical light curve suggests that the blazar undergoes an accretion flare phase, which could

³ The factor 3.92 corresponds to the peak of thermal emission in a νF_{ν} spectrum, obtained by solving $\frac{d}{dx} \frac{x^4}{e^x - 1} = 0$.

⁴ The early-time component could arise from an anisotropic or irregular dust distribution along the line of sight (Yuan et al. 2024), or from pre-existing dust clumps around the SMBH (Jiang et al. 2019a).

lead to the enhanced particle acceleration. Noting that the accretion disk is likely the dominant source of AGN thermal optical emission, we assume that the accretion rate $\dot{M}(t)$ aligns with the optical light curve and define the accretion rate at the peak time of the optical emission, t_{pk} , as \dot{M}_{pk} . We then parametrize the luminosity of injected protons, L_p , as a fraction of the accretion power, i.e., $L_p = \epsilon_p \dot{M} c^2$, where an efficient proton injection efficiency of $\epsilon_p = 0.2$ is adopted as a fiducial value, motivated by the studies of TDEs (Winter & Lunardini 2023). Possible particle acceleration sites include the accretion disk, corona, disk wind, or inner jets. In this work, however, we do not specify the exact acceleration mechanism; instead, we assume particle injection into the isotropic radiation zone characterized by R_{IR} and consider subsequent interactions with isotropized target photons.

We assume a power-law proton injection rate, given by $\dot{Q}_p \propto \epsilon_p^{-s} \exp(-\epsilon_p/\epsilon_{p,\text{max}})$, and normalize the spectrum via $\int \epsilon_p \dot{Q}_p d\epsilon_p = L_p/V$, where $s = 2$ is the spectral index, $\epsilon_{p,\text{max}}$ is the maximum proton energy and $V = 4\pi R_{\text{IR}}^3/3$ is the volume of the radiation zone. We assume a typical magnetic field strength of $B \sim 0.1$ G,⁵ and will show later that the maximum proton energy $\epsilon_{p,\text{max}}$ can reach $\sim 10^9 - 10^{10}$ GeV.

After being injected into the radiation zone, the energetic protons interact with the isotropized thermal optical and IR photons via the $p\gamma$ process, as well as with ambient wind protons via the pp process. We also note that satisfying the $p\gamma$ threshold implies proton energies that are high enough to interact with IR target photons. Both the early-time and the spherical dust torus IR components could contribute to $p\gamma$ interactions. We estimate the free-escaping optical depths at $\epsilon_p \sim 4 \times 10^8$ GeV for $p\gamma$ and pp processes as

$$\tau_{p\gamma} \approx \frac{3\sigma_{p\gamma} L_{\text{IR}}}{4\pi R_{\text{IR}} c \epsilon_{\text{IR}}} \simeq 1.6 L_{\text{IR},44} R_{\text{IR},18}^{-1} \left(\frac{\epsilon_{\text{IR}}}{0.16 \text{ eV}} \right)^{-1} \quad (2)$$

and

$$\begin{aligned} \tau_{pp} &\approx \frac{\eta_w \sigma_{pp} \dot{M}}{4\pi R_{\text{IR}} v_w m_p} \\ &\simeq 1.3 \times 10^{-5} R_{\text{IR},18}^{-1} \beta_{w,-1}^{-1} \dot{M}_{-7}, \end{aligned} \quad (3)$$

where $\sigma_{p\gamma} \simeq 500 \mu\text{b}$ is the $p\gamma$ cross section at Δ -resonance, $\sigma_{pp} \simeq 40 \text{ mb}$ is the pp cross section (Kafexhiu et al. 2014), $\eta_w \sim 10^{-3} - 10^{-1}$ represents the fraction of accreted mass converted to the wind (see

e.g., Ohsuga et al. 2009; Jiang et al. 2019b), the typical wind velocity $v_w = 0.1c$ is used for wind launched from the disk (e.g., Yuan et al. 2020), and the accretion rate is written as $\dot{M} = 10^{-7} \dot{M}_{-7} M_{\odot} \text{ s}^{-1}$. The relation $\tau_{p\gamma} \gg \tau_{pp}$ demonstrates that $p\gamma$ interactions dominate the proton cooling and pion production, as expected in radiation-dense environments. This conclusion holds even for an optimistic wind loading efficiency $\eta_w = 0.1$. In the following calculations, we focus on the neutrinos and other secondary particles produced via $p\gamma$ photomeson process.

The resulting charged (π^{\pm}) and neutral pions (π^0) could decay into neutrinos, γ -rays, and secondary electrons/positrons. These secondary particles, together with electron-positron pairs generated from $\gamma\gamma$ annihilation and Bethe-Heitler (BH) interactions, subsequently initiate EM cascade emissions via synchrotron and inverse Compton radiation. A fully time-dependent modeling of particle injection, cooling, and escape is necessary to accurately describe these nonlinear EM cascades. We use the open-source software AM³ (Astrophysical Multi-Messenger Modeling; Klinger et al. 2024) to solve the coupled transport equations for all relevant particle species. A detailed description of the transport equations can be found in Yuan & Winter (2023) and Klinger et al. (2024). The maximum proton energy, $\epsilon_{p,\text{max}}$, is determined by the physical properties of the acceleration zone. Here, we estimate the maximum proton energy assuming that protons are initially accelerated or re-accelerated in the wind reaching to R_{IR} , by equating the $p\gamma$ cooling rate to the characteristic acceleration rate, given by $t_{\text{acc}}^{-1} = \eta_{\text{acc}} e B c / \epsilon_p$, where $\eta_{\text{acc}} \lesssim 1$ is the acceleration efficiency. Even if the protons are not initially accelerated in the wind, they could still be energized to $\epsilon_{p,\text{max}}$ by the wind diffusive shocks and we will continue to use $\epsilon_{p,\text{max}}$ as a reference in the following discussions.

The AM³ software works with the particle density spectra $n_i = d^2 N_i / dV d \ln \epsilon_i$, where $i = p, e, \gamma, \nu$ respectively represent protons, electrons/positrons, photons, and neutrinos. The photon and neutrino spectra can be converted to the flux in the observer's frame via

$$\nu F_{\nu}(T_{\text{obs}}, E_i) = c \frac{R_{\text{IR}}^2}{3d_L^2} \epsilon_i n_i(\epsilon_i) \Big|_{T_{\text{obs}}/t = \epsilon_i/E_i = 1+z}. \quad (4)$$

For γ -rays, an additional correction factor $\exp[-\tau_{\text{EBL}}(z, E_{\gamma})]$ should be multiplied to Eq. 4 to account for the $\gamma\gamma$ absorption with the extragalactic background light (EBL) during propagation through the Universe, where τ_{EBL} is the optical depth as a function of redshift and photon energy.

This work focuses on the radiation processes in the isotropic radiation zone embedded in the dust torus,

⁵ This value is consistent with the magnetic field strength of the disk-driven winds on sub-parsec scale in AGNs (e.g., Konigl & Kartje 1994; Fukumura et al. 2014).

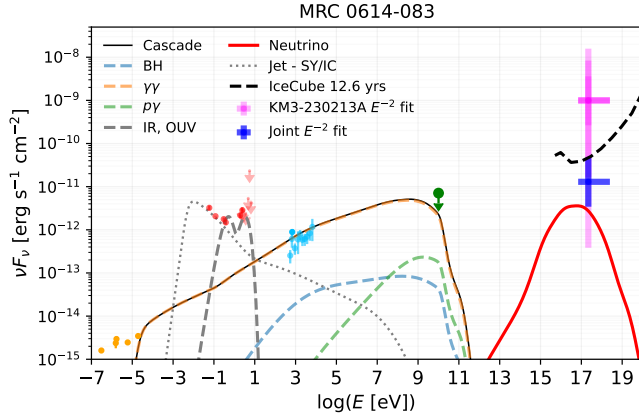


Figure 2. Neutrino and cascade spectra at the neutrino detection time T_ν for the $z = 0.5$ case. The orange, red, blue, and green points represent the radio, infrared/optical/UV, X-ray, and γ -ray observations, respectively. The magenta point denotes the average neutrino flux derived from the KM3-230213A E^{-2} fit, while the dark blue point shows the neutrino flux from the joint E^{-2} fit. The upper limit from the 12.6-year IceCube search is shown as the black dashed curve. The solid black and red curves indicate the total cascade emission and the single-flavor neutrino flux, respectively. The gray dashed curve represents the target photon spectrum, and the black dotted curve shows the jet contribution. Data sources are listed in the main text.

however the blazar relativistic jet may also contribute to the multi-wavelength emissions. The blazar blob leptonic model describes high-energy emission from a relativistic jet in a blazar, where a compact region (or “blob”) of plasma containing relativistic electrons moves along the jet axis. In this model, the observed emission is primarily produced through synchrotron radiation and inverse Compton scattering. Key parameters include bulk Lorentz factor Γ , comoving blob size R'_b , magnetic field strength B'_b , electron luminosity L'_e , spectral index s_b , maximum and minimum Lorentz factors, $\gamma_{e,\max}$ and $\gamma_{e,\min}$. We treat the jet contribution independently and will later show that it may account for the microwave and far-infrared observations.

3.2. Results for the $z = 0.5$ case

We simulate the photomeson production and subsequent EM cascades in the SMBH-rest frame from $t_{\text{start}} = T_{\text{start}}/(1+z)$ to $t_{\text{stop}} = T_{\text{stop}}/(1+z)$ to interpret the X-ray light curves and spectra, and to investigate the possibility of reproducing the UHE neutrino measurements. The starting time, $T_{\text{start}} = 58400$ MJD, and stop time, $T_{\text{stop}} = 60800$ MJD, are chosen to encompass the optical flare, neutrino detection (see the vertical dashed orange line in Fig. 1), and the latest X-ray observations. In this calculation, the peak accretion rate,

\dot{M}_{pk} , is treated as a free parameter, whereas fiducial values are adopted for magnetic field strength $B = 0.1$ G, injection efficiency $\epsilon_p = 0.2$, and the acceleration efficiency $\eta_{\text{acc}} = 1$. Given the redshift, the bolometric IR and X-ray luminosities, as well as the radius of the radiation zone, R_{IR} , are inferred from observations and dust echo fitting. We define the dimensionless peak accretion rate as $\dot{m}_{\text{pk}} = \dot{M}_{\text{pk}}/\dot{M}_{\text{Edd}}$, where \dot{M}_{Edd} is the Eddington accretion rate; this means that $\dot{m}_{\text{pk}} > 1$ refers to super-Eddington accretion. Assuming the SMBH mass of $M = 10^9 M_\odot$ and the radiation efficiency $\eta_{\text{rad}} \sim 0.01 - 0.1$, we have $\dot{M}_{\text{Edd}} \simeq 22 M_\odot \text{ yr}^{-1} M_9 \eta_{\text{rad},-1}^{-1}$.

As a reference, let us first consider the ‘nearby’ blazar case at $z = 0.5$. The fit to the X-ray light curve (see the bottom panel of Fig. 1) and spectrum (see Fig. 2) yields $\dot{m}_{\text{pk}} = 1.3 M_9^{-1} \eta_{\text{rad},-1}$ during the optical flare phase. In the quiescent phase, the accretion rate decreases to $\sim 0.74 M_9^{-1} \eta_{\text{rad},-1}$, consistent with the typical values for powerful blazars, e.g., $\dot{M} \sim 0.1 - 1 \dot{M}_{\text{Edd}}$ (e.g., Ghisellini & Tavecchio 2008; Ghisellini et al. 2009).

The solid black and red curves in Fig. 2 represent the total cascade emission and the single-flavor neutrino spectrum at the neutrino detection time T_ν , respectively, obtained by fitting the X-ray spectra and light curve. The cascade emission consists of the contributions from electrons/positrons produced via $\gamma\gamma$ pair production (orange dashed), $p\gamma$ -induced charged pion decays (green dashed), and the BH pair production (dashed blue). This figure demonstrates that the pair originated from the $\gamma\gamma$ channel dominates the EM cascade, as the $p\gamma$ induced secondary emission (dashed green curve) is significantly suppressed by $\gamma\gamma$ annihilation. The γ -ray upper limit obtained by *Fermi*-LAT is also satisfied, since the internal $\gamma\gamma$ annihilation depletes the secondary γ -rays above 10 GeV. The black solid, magenta dashed, and green dashed-dotted curves in the bottom panel of Fig. 1 show the X-ray (0.2 - 2.3 keV), γ -ray (0.1 - 1000 GeV), and neutrino (above 10 PeV) light curves, respectively, as the outputs of the model.

Notably, the EM cascade emission can simultaneously account for both the X-ray spectrum and the light curve in the energy range 0.2 - 2.3 keV measured by *Swift*-XRT and eROSITA (see the black solid curve in the bottom panel of Fig. 1). The time delay of the X-ray peak relative to the optical peak $\Delta T_X \approx 700 - 800$ d is primarily attributed to the $p\gamma$ interaction timescale $t_{p\gamma}$ which governs the development of EM cascades (see the Fig. 4 in Appendix A). From the left panel of Fig. 4, we read that IR photons dominate $p\gamma$ interactions, which implies that ΔT_X is determined by the $p\gamma$ interaction time scale and the time delay of IR emissions,

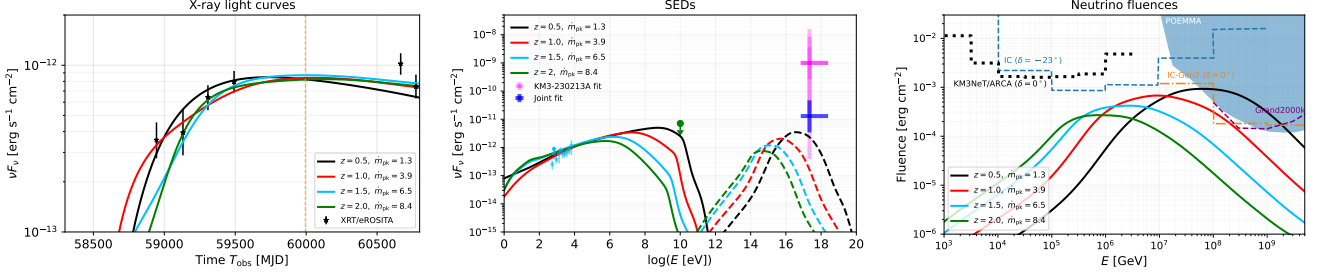


Figure 3. Impact of source redshift on model predictions, with z varied from 0.5 (black curves), 1.0 (red), 1.5 (blue), to 2.0 (green). The left and middle panels show the X-ray light curve fits and spectral fits, respectively. The data points are the same as those in Fig. 1 and Fig. 2. In the middle panel, solid curves represent cascade emissions, while dashed curves indicate the corresponding single-flavor neutrino fluxes. The right panel shows the cumulative single-flavor neutrino fluence up to T_ν . The 90% CL sensitivity curves of neutrino current and future detectors are also included.

e.g., $\Delta T_X \lesssim \max[(1+z)t_{p\gamma}, \Delta T_{\text{IR}}]$. Consequently, our model naturally explains the later emerging X-ray observation together with the X-ray spectra.

For the $z = 0.5$ case, the neutrino spectrum peaks at $E_\nu \simeq 100$ PeV, with a flux reaching 4×10^{-12} erg s $^{-1}$ cm $^{-2}$, which is close to the flux of joint E^{-2} fit with the IceCube measurements at lower energies (see the deep blue point in Fig. 2; Adriani et al. 2025c) and lies within the 3σ flux uncertainty of the KM3-230213A E^{-2} fit (magenta point; Aiello et al. 2025). The upper limit from the 12.6-year IceCube search (Abbasi et al. 2025) is also shown as the black dashed curve for reference. We thus conclude that the blazar MRC 0614-083 could be a promising UHE neutrino emitter. We further verify that this source could accelerate protons to UHEs if the wind serves as the accelerator by evaluating the maximum proton energy $\varepsilon_{p,\text{max}}$. Here, we consider the $\varepsilon_{p,\text{max}}$ that protons can reach inside the radiation zone, via wind shock acceleration (if the wind serves as the accelerator) or re-acceleration (if the protons are accelerated by other structures in the wind). Balancing the $p\gamma$ cooling rate $t_{p\gamma,c}^{-1} = \kappa_{p\gamma} t_{p\gamma}^{-1}$ with the diffusive shock acceleration rate t_{acc}^{-1} (shown as the black line in the left panel of Fig. 4), where $\kappa_{p\gamma} \sim 0.2$ is the inelasticity, we estimate $\varepsilon_{p,\text{max}} \gtrsim 10^{10}$ GeV as a good reference, similar to neutrino-emitting TDEs (Plotko et al. 2024). The resulting neutrino spectrum peaks at $E_{\nu,\text{pk}} \sim 0.05E_{p,\text{max}} \sim 100$ PeV, where $E_{\nu,0}$ is the energy that maximizes the ratio $t_{p\gamma,c}^{-1}/t_{\text{esc}}^{-1}$, and t_{esc} represents the escape timescale of charged particles. While $p\gamma$ interactions between UHE protons and IR photons dominate the production of the highest-energy neutrinos, interactions with optical photons are primarily responsible for extending the neutrino spectrum down to the 100 TeV – PeV range.

The low-energy tail of the EM cascade emission remains consistent with the radio measurement, as the

observed spectrum steepening is caused by synchrotron self-absorption (SSA). The SSA break energy, $E_{\text{SSA}} = \varepsilon_{\text{SSA}}/(1+z) \sim 2.4 \times 10^{-5}$ eV, agrees with the radio upper limits shown in Fig. 2, where $\varepsilon_{\text{SSA}} \sim 3.6 \times 10^{-5}$ eV is determined by the condition $t_{\text{SSA}}^{-1}/t_{\text{fs}}^{-1} = 1$ (see the right panel of Fig. 4). In this expression, $t_{\text{fs}} = R_{\text{IR}}/c$ is the free escaping time for photons and neutrinos.

However, we note that the isotropic EM cascade emission predicted by the accretion flare model alone cannot fully account for the microwave and far-infrared data points in Fig. 2 (specifically, the two red points below 0.1 eV). These features are likely attributable to non-thermal emission from the relativistic jet. To illustrate this possibility, we adopt a leptonic blazar blob model that reproduces these low-frequency data points without delving into model details. The gray dotted curve in Fig. 2 shows the synchrotron and inverse Compton emission, obtained using the following parameters: $\Gamma = 10$, $R'_b = 10^{16}$ cm, $L'_e = 3.5 \times 10^{44}$ erg s $^{-1}$, $s_b = 2.3$, $\gamma'_{e,\text{min}} = 10$, $\gamma'_{e,\text{max}} = 10^3$, and $B'_b = 5$ G.

3.3. Redshift dependence

So far, we have presented a comprehensive time-domain multi-messenger analysis of MRC 0614-083, assuming a redshift of $z = 0.5$. For completeness, we now investigate the dependence of our results on redshift by varying z from 0.5 to 2.0. In this calculation, the peak accretion rate \dot{m}_{pk} is treated as a free parameter, while L_{IR} , L_{Opt} , and R_{IR} are self-consistently determined for each redshift. All other model parameters are held fixed. The corresponding fits to the X-ray light curves and spectra are shown in the left and middle panels of Fig. 3. To reproduce the observed X-ray features at higher redshifts, the source must be a more powerful accretor, with \dot{m}_{pk} increasing from 1.3 to 8.4 as z increases from 0.5 to 2.0.

The right panel of Fig. 3 depicts the cumulative single-flavor neutrino fluence until T_ν for each redshift. The

Table 1. Expected neutrino event numbers and the tension with IceCube non-detection

z	$\mathcal{N}_{\nu, \text{KM3}}$	$\mathcal{N}_{\nu, \text{IC}}$	$P(\text{KM3} \setminus \text{IC})$	Tension [σ]
0.5	0.024	0.76	1.1%	2.30
1.0	0.038	1.34	0.95%	2.34
1.5	0.031	1.14	0.95%	2.34
2.0	0.018	0.72	0.85%	2.39

90% CL sensitivity curves for various neutrino observatories, including IceCube, IceCube-Gen2 (Abbasi et al. 2021), GRAND (Álvarez-Muñiz et al. 2020), POEMMA (Venters et al. 2020), and KM3NeT/ARCA230 (Aiello et al. 2024) are also shown. A notable trend is the redshift-dependent shift of the neutrino spectral peak from ~ 100 PeV at $z = 0.5$ to ~ 1.5 PeV at $z = 2.0$, consistent with expectations in the $p\gamma$ calorimetric regime, where $\kappa_{p\gamma} t_{p\gamma}^{-1} / t_{\text{esc}}^{-1} \gtrsim 1$.

This redshift dependence can be understood as follows: as z increases, the volume of the radiation zone decreases as $R_{\text{IR}}^3 \propto (1+z)^{-3}$, while the IR/X-ray luminosities increase as $L_{X/\text{IR}} \propto d_L^2$. Consequently, the $p\gamma$ cooling rate scales as $t_{p\gamma, c}^{-1} \propto (1+z)^3 d_L(z)^2$. In this case, the maximum proton energy limits the neutrino peak energy in the way: $\varepsilon_{\nu, \text{pk}} \propto \varepsilon_{p, \text{max}} \propto t_{p\gamma, c} \propto (1+z)^{-3} d_L(z)^{-2}$. We derive the expected neutrino peak energy in the observer’s frame

$$E_{\nu, \text{pk}} = \frac{\varepsilon_{\nu, \text{pk}}}{1+z} \propto (1+z)^{-4} d_L(z)^{-2}, \text{ for } \frac{\kappa_{p\gamma} t_{p\gamma}^{-1}}{t_{\text{esc}}^{-1}} \gtrsim 1. \quad (5)$$

This analytic relation provides a reasonable explanation for the observed spectral shift. We conclude that if the source is located at higher redshift, the isotropic radiation zone becomes increasingly inefficient in producing UHE neutrinos. In these cases, alternative zones, such as relativistic jet blobs, may play a more dominant role in neutrino production. However, a detailed exploration of such jet scenarios is beyond the scope of this work.

4. DISCUSSION

We have demonstrated that the accretion flare scenario can explain the time-dependent multi-wavelength observations of MRC 1614-083 and is capable of producing UHE neutrinos at a flux level consistent with the joint E^{-2} spectral fit. To assess the observational prospects, it is useful to evaluate the detectability by both KM3NeT and IceCube. The UHE neutrino event KM3-230213 arrived from a near-horizontal direction to KM3NeT, corresponding to approximately 8° above the horizon at IceCube – still within IceCube’s optimal performance range. In this direction, the IceCube’s effective

area is larger than KM3NeT, which leads to a tension for the non-detection by IceCube even for transients. Using the KM3NeT horizontal effective area (Caiffi et al. 2024; Li et al. 2025) and IceCube effective area 8° above the horizon (Aartsen et al. 2014), we estimate the expected neutrino number ($\mathcal{N}_{\nu, \text{KM3/IC}}$ for KM3NeT/IceCube) to be

$$\mathcal{N}_\nu = \int dE_\nu \int_{T_{\text{start}}}^{T_\nu} dT A_{\text{eff}}(E_\nu) F_\nu(T, E_\nu), \quad (6)$$

where A_{eff} is the effective area. For KM3NeT, $T_{\text{start}} = T_\nu - 288$ d is used noting that the exposure time is 288 days. We consider a Poissonian possibility for the KM3NeT detection with IceCube non-detection $P(\text{KM3} \setminus \text{IC}) = \mathcal{N}_{\nu, \text{KM3}} \exp(-\mathcal{N}_{\nu, \text{KM3}}) \exp(-\mathcal{N}_{\nu, \text{IC}})$. This probability can be translated into a confidence level for the tension, assuming a Gaussian distribution. Table 1 summarizes the expected neutrino numbers for KM3NeT and IceCube, as well as $P(\text{KM3} \setminus \text{IC})$ and the tension confidence levels. The results indicate that for the accretion flare scenario would lead to a tension of $\sim 2.3 - 2.4\sigma$, which is consistent with the expected values for point sources and lower compared to the tension associated with a diffuse isotropic neutrino origin or the cosmogenic scenario ($3.1 - 3.6\sigma$; Li et al. 2025).

Regarding the expected number of neutrino events for IceCube, \mathcal{N}_{IC} , discussed earlier, the integration begins at $T_{\text{start}} = 58400$ MJD. In reality, however, neutrino production could have occurred during the ‘steady’ accretion phase prior to T_{start} . Given the ~ 1000 -day gap without optical or X-ray observations, we estimate the maximum possible contribution from this steady phase, extending back to the start of IceCube operations. As shown in the lower panel of Fig. 1, the neutrino light curve closely follows the X-ray light curve. We therefore assume that both the X-ray and neutrino fluxes remained at a constant level prior to 58900 MJD. Under this assumption, the values of \mathcal{N}_{IC} listed in Table 1 should be rescaled by a factor of ~ 2.1 to account for neutrino production during this extended period. This implies an increased tension with IceCube’s non-detection, at the level of $2.6 - 2.7\sigma$, though still below the tension expected in cosmogenic scenarios. On the other hand, the absence of X-ray emission during the steady phase may indicate a lower baryon loading, in which case the tension would converge to the values inferred from the flare phase, i.e., $2.3 - 2.4\sigma$.

One principal uncertainty in the accretion flare model arises from the lack of redshift measurements. The dust echo fitting and multimessenger modeling presented in the previous Section suggest that the isotropic radiation zone can account for the infrared, X-ray, and γ -ray observations by increasing only the peak accretion

rate, \dot{m}_{pk} , from 1.3 to 8.4, without altering other fiducial parameters, as the redshift increases from $z = 0.5$ to $z = 2.0$. This required values of \dot{m}_{pk} also depend on the SMBH mass, which is not determined from current observations as well. Qualitatively, a super-Eddington accretion flare is generally needed even for the efficient proton injection case, e.g., $\epsilon_p = 0.2$, and the source should be increasingly powerful if it locates at a higher redshift. As z increases, the peak neutrino energies shift from ~ 100 PeV to ~ 1 PeV, making it difficult to explain the detection of ultra-high-energy neutrinos by KM3NeT. In such a scenario, the relativistic jet with a high Lorentz factor would play an increasingly important role, motivating a lepto-hadronic modeling of the multimessenger emission from MRC 1614-083. Nevertheless, the relativistic jet contribution would be stringently constrained by the γ -ray upper limits.

The EM cascade emission accounts for the X-ray observations and remains consistent with the *Fermi* γ -ray upper limits throughout the duration of the flare. This conclusion is not highly sensitive to the magnetic field strength, as secondary electrons efficiently lose energy to the radiation field via synchrotron radiation and inverse Compton scattering. The high- and low-energy cutoffs of the EM spectrum are determined by in-source $\gamma\gamma$ attenuation and synchrotron self-absorption, respectively. For the neutrino spectrum, a stronger magnetic field can offset the redshift-induced energy shift. However, achieving high magnetization in an isotropic, non-relativistic region of radius $10^{17} - 10^{18}$ cm is nontrivial. On the other hand, we have focused on the EM cascades induced by $p\gamma$ interactions, without taking into account the EM emissions from primary electrons, in order to maximize the neutrino productions. Yuan & Winter (2023) pointed out that the EM cascade would dominate the multi-wavelength emission if the power of injected electrons is two orders of magnitude lower than the proton power, e.g., $L_e/L_p \lesssim 10^{-2}$. This condition is generally satisfied for non-relativistic diffusive shock accelerations (e.g. Jones 2011; Morlino & Caprioli 2012).

5. SUMMARY AND CONCLUSIONS

In this work, we propose a fully time-dependent accretion flare interpretation of the UHE neutrino event KM3-230213A in association with its directionally closest source, the AGN blazar MRC 1614-083. The flare could originate from various processes, such as a TDE occurring within the AGN environment or a temporary enhancement in accretion due to the infall of molecular gas. Our generic picture is a phase of (moderately) super-Eddington mass accretion leading to the observed optical flare, followed by partially delayed emission of

IR radiation (dust echoes) from re-processed radiation in dust surrounding the SMBH.

While we cannot directly infer the proton acceleration site, the injection of non-thermal protons in an isotropic wind and their interaction with the infrared photons from the dust echoes leads to

- A neutrino signal correlated with the delayed dust echo, explaining the delay of the neutrino emission with respect to the peak mass accretion rate.
- An electromagnetic cascade driven by π^0 gamma-rays, which nicely describes the observed X-ray flare both as a function of time and the spectrum.

Our obtained UHE neutrino peak energy ~ 100 PeV is consistent with *Fermi* γ -ray upper limits while simultaneously fitting the X-ray data. The obtained neutrino flux is consistent with the level predicted by the joint E^{-2} fit in combination with IceCube, provided the source is close enough (e.g., $z \lesssim 1.0$). Moreover, given the source’s variability and the fact that neutrino production reaches a high level near the time of the neutrino detection, the tension with IceCube’s non-detection can be alleviated to a significance of $\sim 2.3 - 2.4\sigma$ (or $\lesssim 2.6 - 2.7\sigma$ if the steady state prior to the flare phase is also considered), regardless of the redshift.

In conclusion, MRC 1614-083 emerges as an interesting candidate for the origin of KM3-230213A due to its proximity (it is the only blazar within the neutrino’s 68% CL directional region) and its capability of producing UHE neutrinos during an accretion flare phase leading to *observed* dust echoes (as immediate consequence of the “illuminated” surrounding dust) and an *observed* X-ray flare (as a consequence of electromagnetic cascades associated with neutrino production), such that a self-consistent picture emerges. The measured neutrino energies indicate the acceleration of UHECRs in the EeV range.

We recommend continued multi-wavelength follow-up observations of this source, particularly to determine its redshift and the SMBH mass, as this would enable time-domain tests of our model, facilitate future lepto-hadronic studies of potential contributions from relativistic jets, and help assess the likelihood of its association with KM3-230213A.

ACKNOWLEDGMENTS

We thank Maria Petropoulou for valuable discussions and Georgios Vasilopoulos for providing the XMM-Newton X-ray upper limit at MJD 60410. We thank Damiano F. G. Fiorillo for insightful comments on the manuscript. This work was supported by the European Research Council, ERC Starting grant *MessMapp*, S.B. Principal Investigator, under contract no. 949555.

We acknowledge the use of public data from the Neil Gehrels Swift Observatory data archive and thank the Observation Duty Scientists and the science planners for carrying out our Swift target of opportunity observation (ToO ID: 22343). This work has made use of data from the Asteroid Terrestrial-impact Last Alert System (ATLAS) project. The Asteroid Terrestrial-impact Last Alert System (ATLAS) project is primarily funded to search for near earth asteroids through NASA grants NN12AR55G, 80NSSC18K0284, and 80NSSC18K1575; byproducts of the NEO search include images and catalogs from the survey area. This work was partially funded by Kepler/K2 grant J1944/80NSSC19K0112 and HST GO-15889, and STFC grants ST/T000198/1 and ST/S006109/1. The ATLAS science products have been made possible through the contributions of the Univer-

sity of Hawaii Institute for Astronomy, the Queen's University Belfast, the Space Telescope Science Institute, the South African Astronomical Observatory, and The Millennium Institute of Astrophysics (MAS), Chile. This work is based on observations obtained with the Samuel Oschin Telescope 48-inch and the 60-inch Telescope at the Palomar Observatory as part of the Zwicky Transient Facility project. ZTF is supported by the National Science Foundation under Grant No. AST-2034437 and a collaboration including Caltech, IPAC, the Weizmann Institute for Science, the Oskar Klein Center at Stockholm University, the University of Maryland, Deutsches Elektronen-Synchrotron and Humboldt University, the TANGO Consortium of Taiwan, the University of Wisconsin at Milwaukee, Trinity College Dublin, Lawrence Livermore National Laboratories, and IN2P3, France. Operations are conducted by COO, IPAC, and UW. This publication makes use of data products from the Wide-field Infrared Survey Explorer, which is a joint project of the University of California, Los Angeles, and the Jet Propulsion Laboratory/California Institute of Technology, funded by the National Aeronautics and Space Administration.

APPENDIX

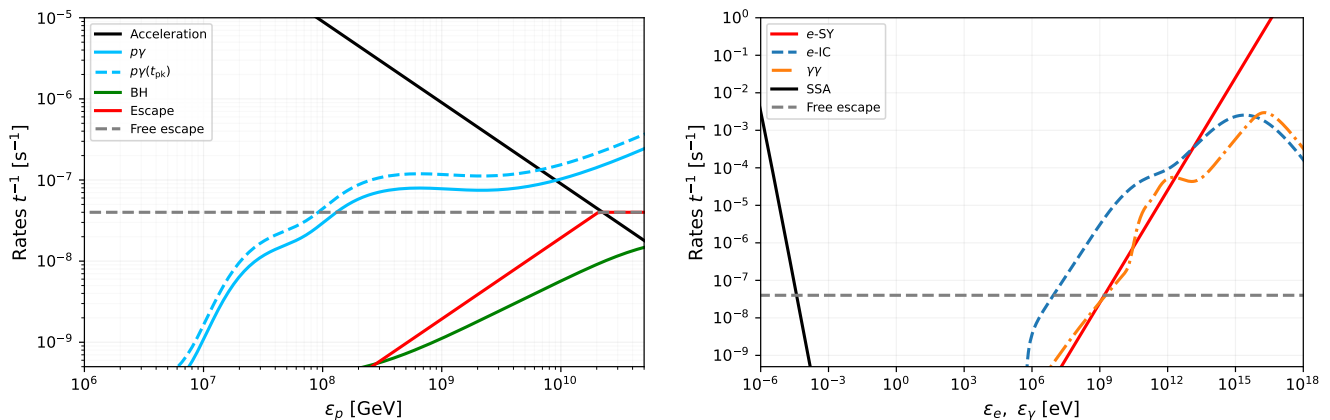


Figure 4. Interaction rates at the neutrino detection time for protons (left panel), photons and secondary electrons/positrons (right panel). Physical quantities are measured in the SMBH-rest frame. Processes in the left panel include particle acceleration (black solid), $p\gamma$ (blue), BetheHeitler pair production (green), particle escape (red solid). The right panel shows rates for $\gamma\gamma$ attenuation (orange dashed-dotted), synchrotron cooling (red solid), inverse Compton scattering (dark blue dashed), and synchrotron self-absorption (black solid). The horizontal gray dashed lines represent the free escape rates.

A. INTERACTION RATES

In Fig. 4, we present the interaction rates for protons (left panel), photons and secondary electrons (right panel). All of the rates are obtained at the neutrino detection time except for the dashed blue curve in the left panel, which corresponds to the peak time of the optical emission t_{pk} . From the left panel, we conclude that the acceleration of UHE protons with energies up to $\sim 10^{10}$ GeV is allowed by equating the loss rate to the accelerate rate, e.g., $\kappa_{p\gamma} t_{p\gamma}^{-1} + t_{\text{esc}}^{-1} = t_{\text{acc}}^{-1}$, where $\kappa_{p\gamma} \sim 0.2$ is the inelasticity, t_{esc}^{-1} is the escape rate (red curve), and t_{acc}^{-1} is the accelerate rate with $\eta_{\text{acc}} = 1$ (black curve). Applying the Bohm limit, the escape rate can be written as $t_{\text{esc}}^{-1} = \min[D/R_{\text{IR}}^2, t_{\text{fs}}^{-1}]$ (Baerwald et al. 2013), where $D = \varepsilon_p c / eB$ is the diffusion coefficient and $t_{\text{fs}}^{-1} = c/R_{\text{IR}}$ is the free-escaping rate.

The electron interaction rates shown in the right panel indicate that inverse Compton scattering dominates the development of the EM cascades. In this regime, the resulting cascade spectrum follows a universal form, $\nu F_\nu \propto E_\gamma^{1/2}$ (Berezinsky & Kalashev 2016), which is consistent with the numerical results (see the EM cascade spectra in Figs. 2 and 3).

REFERENCES

- Aartsen, M. G., et al. 2014, *Astrophys. J.*, 796, 109, doi: [10.1088/0004-637X/796/2/109](https://doi.org/10.1088/0004-637X/796/2/109)
- Abbasi, R., et al. 2021, *PoS, ICRC2021*, 1183, doi: [10.22323/1.395.1183](https://doi.org/10.22323/1.395.1183)
- . 2025. <https://arxiv.org/abs/2502.01963>
- Adrian-Martinez, S., et al. 2016, *J. Phys. G*, 43, 084001, doi: [10.1088/0954-3899/43/8/084001](https://doi.org/10.1088/0954-3899/43/8/084001)
- Adriani, O., et al. 2025a. <https://arxiv.org/abs/2502.08387>
- . 2025b. <https://arxiv.org/abs/2502.08484>
- . 2025c. <https://arxiv.org/abs/2502.08173>
- Aiello, S., Albert, A., Alshamsi, M., et al. 2024, *Astroparticle Physics*, 162, 102990, doi: [10.1016/j.astropartphys.2024.102990](https://doi.org/10.1016/j.astropartphys.2024.102990)
- Aiello, S., et al. 2025, *Nature*, 638, 376, doi: [10.1038/s41586-024-08543-1](https://doi.org/10.1038/s41586-024-08543-1)
- Álvarez-Muñiz, J., Alves Batista, R., Balagopal V., A., et al. 2020, *Science China Physics, Mechanics, and Astronomy*, 63, 219501, doi: [10.1007/s11433-018-9385-7](https://doi.org/10.1007/s11433-018-9385-7)
- Baerwald, P., Bustamante, M., & Winter, W. 2013, *Astrophys. J.*, 768, 186, doi: [10.1088/0004-637X/768/2/186](https://doi.org/10.1088/0004-637X/768/2/186)
- Berezinsky, V., & Kalashev, O. 2016, *Phys. Rev. D*, 94, 023007, doi: [10.1103/PhysRevD.94.023007](https://doi.org/10.1103/PhysRevD.94.023007)
- Bonvin, V., Courbin, F., Suyu, S. H., et al. 2017, *MNRAS*, 465, 4914, doi: [10.1093/mnras/stw3006](https://doi.org/10.1093/mnras/stw3006)
- Burrows, D. N., et al. 2005, *Space Sci. Rev.*, 120, 165, doi: [10.1007/s11214-005-5097-2](https://doi.org/10.1007/s11214-005-5097-2)
- Caiffi, B., et al. 2024, Combined diffuse and point source search with KM3NeT/ARCA and ANTARES neutrino telescopes, Poster
- Condon, J. J., Cotton, W. D., Greisen, E. W., et al. 1998, *AJ*, 115, 1693, doi: [10.1086/300337](https://doi.org/10.1086/300337)
- Das, S., Zhang, B., Razzaque, S., & Xu, S. 2025. <https://arxiv.org/abs/2504.10847>
- Drake, A. J., Djorgovski, S. G., Mahabal, A., et al. 2009, *ApJ*, 696, 870, doi: [10.1088/0004-637X/696/1/870](https://doi.org/10.1088/0004-637X/696/1/870)
- Dzhatdоеv, T. A. 2025. <https://arxiv.org/abs/2502.11434>
- Fang, K., Halzen, F., & Hooper, D. 2025, *Astrophys. J. Lett.*, 982, L16, doi: [10.3847/2041-8213/adbbec](https://doi.org/10.3847/2041-8213/adbbec)
- Fiorillo, D. F. G., Comisso, L., Peretti, E., Petropoulou, M., & Sironi, L. 2024, *Astrophys. J.*, 974, 75, doi: [10.3847/1538-4357/ad7021](https://doi.org/10.3847/1538-4357/ad7021)
- Fitzpatrick, E. L. 1999, *PASP*, 111, 63, doi: [10.1086/316293](https://doi.org/10.1086/316293)
- Fukumura, K., Tombesi, F., Kazanas, D., et al. 2014, *ApJ*, 780, 120, doi: [10.1088/0004-637X/780/2/120](https://doi.org/10.1088/0004-637X/780/2/120)
- Ghisellini, G., Righi, C., Costamante, L., & Tavecchio, F. 2017, *MNRAS*, 469, 255, doi: [10.1093/mnras/stx806](https://doi.org/10.1093/mnras/stx806)
- Ghisellini, G., & Tavecchio, F. 2008, *MNRAS*, 387, 1669, doi: [10.1111/j.1365-2966.2008.13360.x](https://doi.org/10.1111/j.1365-2966.2008.13360.x)
- Ghisellini, G., Tavecchio, F., & Ghirlanda, G. 2009, *MNRAS*, 399, 2041, doi: [10.1111/j.1365-2966.2009.15397.x](https://doi.org/10.1111/j.1365-2966.2009.15397.x)
- Gordon, Y. A., Boyce, M. M., O’Dea, C. P., et al. 2021, *ApJS*, 255, 30, doi: [10.3847/1538-4365/ac05c0](https://doi.org/10.3847/1538-4365/ac05c0)
- Hale, C., McConnell, D., Thomson, A., et al. 2021, *Publications of the Astronomical Society of Australia*, 38, 1, doi: [10.1017/pasa.2021.47](https://doi.org/10.1017/pasa.2021.47)
- Jiang, N., Dou, L., Wang, T., et al. 2016, *ApJ*, 828, L14, doi: [10.3847/2041-8205/828/1/L14](https://doi.org/10.3847/2041-8205/828/1/L14)
- Jiang, N., Wang, T., Mou, G., et al. 2019a, *ApJ*, 871, 15, doi: [10.3847/1538-4357/aaf6b2](https://doi.org/10.3847/1538-4357/aaf6b2)
- Jiang, Y.-F., Stone, J. M., & Davis, S. W. 2019b, *ApJ*, 880, 67, doi: [10.3847/1538-4357/ab29ff](https://doi.org/10.3847/1538-4357/ab29ff)
- Jones, T. W. 2011, *Journal of Astrophysics and Astronomy*, 32, 427, doi: [10.1007/s12036-011-9128-y](https://doi.org/10.1007/s12036-011-9128-y)
- Kafexhiu, E., Aharonian, F., Taylor, A. M., & Vila, G. S. 2014, *Phys. Rev. D*, 90, 123014, doi: [10.1103/PhysRevD.90.123014](https://doi.org/10.1103/PhysRevD.90.123014)

- Klinger, M., Rudolph, A., Rodrigues, X., et al. 2024, *Astrophys. J. Suppl.*, 275, 4, doi: [10.3847/1538-4365/ad725c](https://doi.org/10.3847/1538-4365/ad725c)
- Konigl, A., & Kartje, J. F. 1994, *ApJ*, 434, 446, doi: [10.1086/174746](https://doi.org/10.1086/174746)
- Lane, W. M., Cotton, W. D., van Velzen, S., et al. 2014, *MNRAS*, 440, 327, doi: [10.1093/mnras/stu256](https://doi.org/10.1093/mnras/stu256)
- Large, M. I., Cram, L. E., & Burgess, A. M. 1991, *The Observatory*, 111, 72
- Li, R.-L., Yuan, C., He, H.-N., et al. 2024, <https://arxiv.org/abs/2411.06440>
- Li, S. W., Machado, P., Naredo-Tuero, D., & Schwemberger, T. 2025, <https://arxiv.org/abs/2502.04508>
- Liu, R.-Y., Murase, K., Inoue, S., Ge, C., & Wang, X.-Y. 2018, *Astrophys. J.*, 858, 9, doi: [10.3847/1538-4357/aaba74](https://doi.org/10.3847/1538-4357/aaba74)
- Lu, W., Kumar, P., & Evans, N. J. 2016, *MNRAS*, 458, 575, doi: [10.1093/mnras/stw307](https://doi.org/10.1093/mnras/stw307)
- Mainzer, A., Bauer, J., Grav, T., et al. 2011, *ApJ*, 731, 53, doi: [10.1088/0004-637X/731/1/53](https://doi.org/10.1088/0004-637X/731/1/53)
- Masci, F. J., Laher, R. R., Rusholme, B., et al. 2019, *PASP*, 131, 018003, doi: [10.1088/1538-3873/aae8ac](https://doi.org/10.1088/1538-3873/aae8ac)
- Merloni, A., et al. 2024, *Astron. Astrophys.*, 682, A34, doi: [10.1051/0004-6361/202347165](https://doi.org/10.1051/0004-6361/202347165)
- Morlino, G., & Caprioli, D. 2012, *A&A*, 538, A81, doi: [10.1051/0004-6361/201117855](https://doi.org/10.1051/0004-6361/201117855)
- Murase, K., Dermer, C. D., Takami, H., & Migliori, G. 2012, *ApJ*, 749, 63, doi: [10.1088/0004-637X/749/1/63](https://doi.org/10.1088/0004-637X/749/1/63)
- Murase, K., Inoue, Y., & Dermer, C. D. 2014, *Phys. Rev. D*, 90, 023007, doi: [10.1103/PhysRevD.90.023007](https://doi.org/10.1103/PhysRevD.90.023007)
- Murase, K., Kimura, S. S., & Meszaros, P. 2020, *Phys. Rev. Lett.*, 125, 011101, doi: [10.1103/PhysRevLett.125.011101](https://doi.org/10.1103/PhysRevLett.125.011101)
- Murase, K., & Stecker, F. W. 2023, 483, doi: [10.1142/9789811282645_0010](https://doi.org/10.1142/9789811282645_0010)
- Muzio, M. S., Yuan, T., & Lu, L. 2025, <https://arxiv.org/abs/2502.06944>
- Neronov, A., Oikonomou, F., & Semikoz, D. 2025, <https://arxiv.org/abs/2502.12986>
- Ohsuga, K., Mineshige, S., Mori, M., & Kato, Y. 2009, *PASJ*, 61, L7, doi: [10.1093/pasj/61.3.L7](https://doi.org/10.1093/pasj/61.3.L7)
- Plotko, P., Winter, W., Lunardini, C., & Yuan, C. 2024, <https://arxiv.org/abs/2410.19047>
- Rau, A., Schady, P., Greiner, J., et al. 2012, *A&A*, 538, A26, doi: [10.1051/0004-6361/201118159](https://doi.org/10.1051/0004-6361/201118159)
- Reusch, S., et al. 2022, *Phys. Rev. Lett.*, 128, 221101, doi: [10.1103/PhysRevLett.128.221101](https://doi.org/10.1103/PhysRevLett.128.221101)
- Schlafly, E. F., & Finkbeiner, D. P. 2011, *ApJ*, 737, 103, doi: [10.1088/0004-637X/737/2/103](https://doi.org/10.1088/0004-637X/737/2/103)
- Tonry, J. L., Denneau, L., Heinze, A. N., et al. 2018, *PASP*, 130, 064505, doi: [10.1088/1538-3873/aabadf](https://doi.org/10.1088/1538-3873/aabadf)
- van Velzen, S., et al. 2024, *Mon. Not. Roy. Astron. Soc.*, 529, 2559, doi: [10.1093/mnras/stae610](https://doi.org/10.1093/mnras/stae610)
- Venters, T. M., Reno, M. H., Krizmanic, J. F., et al. 2020, *Phys. Rev. D*, 102, 123013, doi: [10.1103/PhysRevD.102.123013](https://doi.org/10.1103/PhysRevD.102.123013)
- Wang, X., & Loeb, A. 2017, *Phys. Rev. D*, 95, 063007, doi: [10.1103/PhysRevD.95.063007](https://doi.org/10.1103/PhysRevD.95.063007)
- Winter, W., & Lunardini, C. 2023, *Astrophys. J.*, 948, 42, doi: [10.3847/1538-4357/acbe9e](https://doi.org/10.3847/1538-4357/acbe9e)
- Wright, A. E., Griffith, M. R., Burke, B. F., & Ekers, R. D. 1994, *ApJS*, 91, 111, doi: [10.1086/191939](https://doi.org/10.1086/191939)
- Wright, E. L., Eisenhardt, P. R. M., Mainzer, A. K., et al. 2010, *AJ*, 140, 1868, doi: [10.1088/0004-6256/140/6/1868](https://doi.org/10.1088/0004-6256/140/6/1868)
- Yuan, C., Murase, K., Kimura, S. S., & Mészáros, P. 2020, *Phys. Rev. D*, 102, 083013, doi: [10.1103/PhysRevD.102.083013](https://doi.org/10.1103/PhysRevD.102.083013)
- Yuan, C., & Winter, W. 2023, *Astrophys. J.*, 956, 30, doi: [10.3847/1538-4357/acf615](https://doi.org/10.3847/1538-4357/acf615)
- Yuan, C., Winter, W., & Lunardini, C. 2024, *Astrophys. J.*, 969, 136, doi: [10.3847/1538-4357/ad50a9](https://doi.org/10.3847/1538-4357/ad50a9)
- Zhang, Q., Huang, T.-Q., & Li, Z. 2025, <https://arxiv.org/abs/2504.10378>